

Nanoscale Chemical Structure-Mechanical Property-Processing Relationships for Nanopatterned Organo-Silicate Fins

Gheorghe Stan,^{1} Richard S. Gates,¹ Qichi Hu,² Kevin Kjoller,^{2**} Craig Prater,² Kanwal Jit Singh,³ Ebony Mays,⁴ Sean W. King^{4***}*

¹Material Measurement Laboratory, National Institute of Standards and Technology, Gaithersburg, MD 20899, USA

²Anasys Instruments Incorporated, Santa Barbara, CA 93101, USA

³Components Research, Intel Corporation, Hillsboro OR 97124, USA

⁴Logic Technology Development, Intel Corporation, Hillsboro OR 97124, USA

* gheorghe.stan@nist.gov; ** kevin@anasysinstruments.com

*** Corresponding author: sean.king@intel.com; Ph: 503-613-7547; Logic Technology

Development, Intel Corporation, 5200 NE Elam Young Parkway, Hillsboro OR 97124, USA

ABSTRACT. The exploitation of nanoscale size effects to create new nanostructured materials will necessitate the simultaneous development of nanoscale molecular structure, physical property, and material processing relationships. Numerous metrologies capable of nanoscale thermal, mechanical, and electrical characterization have been demonstrated in the past two decades. However, the ability to perform nanoscale molecular/chemical structure characterization has only been recently demonstrated with the advent of new atomic force microscope based infrared spectroscopy (AFM-IR) and related techniques. Therefore, we have combined AFM-IR chemical structure and contact resonance AFM (CR-AFM) mechanical property measurements to investigate the fabrication of 20 – 500

nm wide fin structures in a nano-porous organo-silicate material and demonstrate the ultimate goal of nanoscale chemical structure-physical property-material processing characterization. We show that by combining these two techniques, one can clearly observe nanoscale chemical structure and mechanical property variations that correlate with the fabrication process and the feature size of the organo-silicate fins. Specifically, we have observed an inverse correlation between the concentration of terminal organic groups and the stiffness of nano-patterned organo-silicate fins where selective removal of the organic component during etching results in a stiffness increase and reinsertion via chemical silylation results in a stiffness decrease. Examination of this effect as a function of fin width indicates that the loss of terminal organics and stiffness increase occurs primarily at the exposed surfaces of the fins over a length scale of 10-20 nm. While the observed structure-property relationship is specific to organo-silicates, we believe the combined demonstration of AFM-IR with CR-AFM should pave the way for similar nanoscale characterization of other materials where such relationships are essential.

KEYWORDS. atomic force microscope; contact resonance; infrared spectroscopy; organo-silicate; photo-thermal.

INTRODUCTION:

A fundamental objective of materials science and engineering is to understand, control, and exploit the relationship between a material's properties and its structure at various length scales to create new materials with novel functionalities that benefit mankind [1]. To date, the structure-property relationships of various materials have been understood at the macro, micro, and even atomic length scales in a few specific cases [2]. However, nanoscale chemical structure-material property characterization has been experimentally elusive [3] and has become a pervasive need for research currently focussed on manipulating matter at nanometer length scales to take advantage of various nanoscale size effects [4-6]. It is a particularly pressing need for the semiconductor industry where the ability to resolve, map, and create nanoscale variations in chemical structure and material properties will be needed to extend Moore's law transistor scaling into the single digit nanometer regime [7,8]. Nanoscale structure-property characterization of grain boundaries and inter-boundary materials has also been recently identified as one of the current grand challenges for ceramic science research [9]. Numerous other fields of science including chemistry, physics, and biology would additionally benefit from the ability to perform combined nanoscale chemical structure and material property characterization where there is a similar need to understand the structure-functionality relationships of sub-cellular components [10-14].

Interestingly, the dearth of nanoscale chemical structure-material property studies has not been due to the absence of nanoscale material property characterization techniques (there are many thanks to numerous advances in scanned probe microscopy (SPM) [15-21]), but instead due to the non-existence of chemical structure identification techniques with nanometer lateral

(in-plane) spatial resolution. While scatterometry and near-field optical microscopy (NSOM) techniques have allowed sub-wavelength features to be resolved [22,23], the lack of nanoscale chemical structure techniques has largely been due to Abbe diffraction constraints that prohibit direct spatial resolution scaling of light based spectroscopy techniques, such as infrared (IR) absorption spectroscopy, from the micrometer into the nanometer range [24]. Fortunately, these limitations have been recently overcome via combining optical spectroscopy with atomic force microscopy (AFM) and exploiting either near-field optical enhancements produced by the probe tip [25,26], or using the AFM probe to detect various photoinduced thermal-mechanical responses [24,27]. However, these techniques have yet to be routinely combined with other nanoscale SPM material property measurement techniques to provide credible demonstrations of nanoscale structure-property characterization.

In this regard, we provide here a compelling demonstration of nanoscale chemical structure-mechanical property characterization by combining AFM based IR (AFM-IR) [28] spectroscopy with contact resonance AFM (CR-AFM) [29] mechanical property measurements in the investigation of 20 – 500 nm wide fin structures fabricated in a nano-porous organo-silicate thin film. Nano-porous organo-silicates are of significant importance to the nano-electronics industry for reducing various parasitic capacitances [30], but are extremely susceptible to chemical structure and material property modification during processing due to the presence of labile organics and interconnected porosity [31,32]. Using AFM-IR, we have recently been able to observe nanoscale variations in the loss of the organic component in a organo-silicate induced by the plasma etching and ashing processes utilized to transfer lithographically defined features into these materials [32]. Likewise, we have also recently demonstrated the ability of CR-AFM to resolve nanoscale variations in the mechanical stiffness

of organo-silicate materials that have undergone similar but not identical types of processing [33,34]. By combining AFM-IR with CR-AFM in the investigation of the same material, we are now able to clearly demonstrate a correlation between the mechanical stiffness of the nanoporous organo-silicate and the selective removal and reinsertion of terminal organic (CH_3) groups in the matrix. Further examination of this effect as a function of fin width and additional recently demonstrated depth profiling CR-AFM mechanical property measurements [34] indicate that the loss of CH_3 and increase of mechanical stiffness occurs primarily at the exposed top and sidewall surfaces of the fins over a length scale on the order of tens of nanometers. These results provide a relevant demonstration of nanoscale chemical structure-material property characterization and processing correlations for other fields of nanoscale science [9-12].

EXPERIMENTAL:

Fabrication of Nanoporous Fins

The nano-porous organo-silicate fin structures examined in this study were fabricated using a previously described subtractive pitch quartering process [34,35]. Briefly, plasma enhanced chemical vapor deposition (PECVD) was used to deposit a 120 nm thick organo-silicate on a 100 nm SiO_2 thin film previously grown on a 300 mm diameter Si (001) substrate. During deposition of the organo-silicate, a second phase organic pore building “porogen” material was co-incorporated in the organo-silicate film and then sacrificially removed using a UV cure to create a 33% nano-porous organo-silicate material with a nominal Young’s modulus of 5 GPa [36]. The pitch quarter patterning process consisted of first depositing on the nanoporous organo-silicate a quad-layer film stack consisting of a backbone layer, an anti reflection

coating, a second backbone layer and a hard mask. Standard 193 nm immersion lithography and etch techniques were utilized to form a grid pattern in the first backbone layer. A spacer dielectric was then deposited over the backbone grid and the backbone material selectively removed. Standard plasma etch techniques were then utilized to transfer this pattern into the second backbone layer that was subsequently coated with a second spacer material. The remaining second backbone material was subsequently removed and the second spacer pattern transferred into the hard mask material and then into the nano-porous organo-silicate using standard plasma etch techniques. On completion of transferring the pitch quartered pattern into the nano-porous organo-silicate, the remaining hard mask and plasma etch residues were removed using standard plasma ash and wet chemical cleans.

Figure 1 provides schematic illustrations and AFM images of the fin structures examined in this study. The schematic in Figure 1a specifically illustrates that an array of approximately 100 nm tall fins with widths of 20, 90, and 500 nm were fabricated in the organo-silicate. As shown in the AFM image presented in Fig. 1b, the length of the 20 nm wide fins was approximately 500 nm and these fins were nested within the wider 90 and 500 nm wide fins that run in length for more than 5 microns. It can be also observed that the height of the fins decreases by 5-10 nm with decreasing width due to pattern dependent differences in the plasma etch/erosion rate of the photoresist and hardmask layers utilized to define and transfer the desired pattern into the nano-porous organo-silicate [35]. As we will show, feature size dependences also manifest as composition and mechanical property variations within the resulting nano-porous organo-silicate fins.

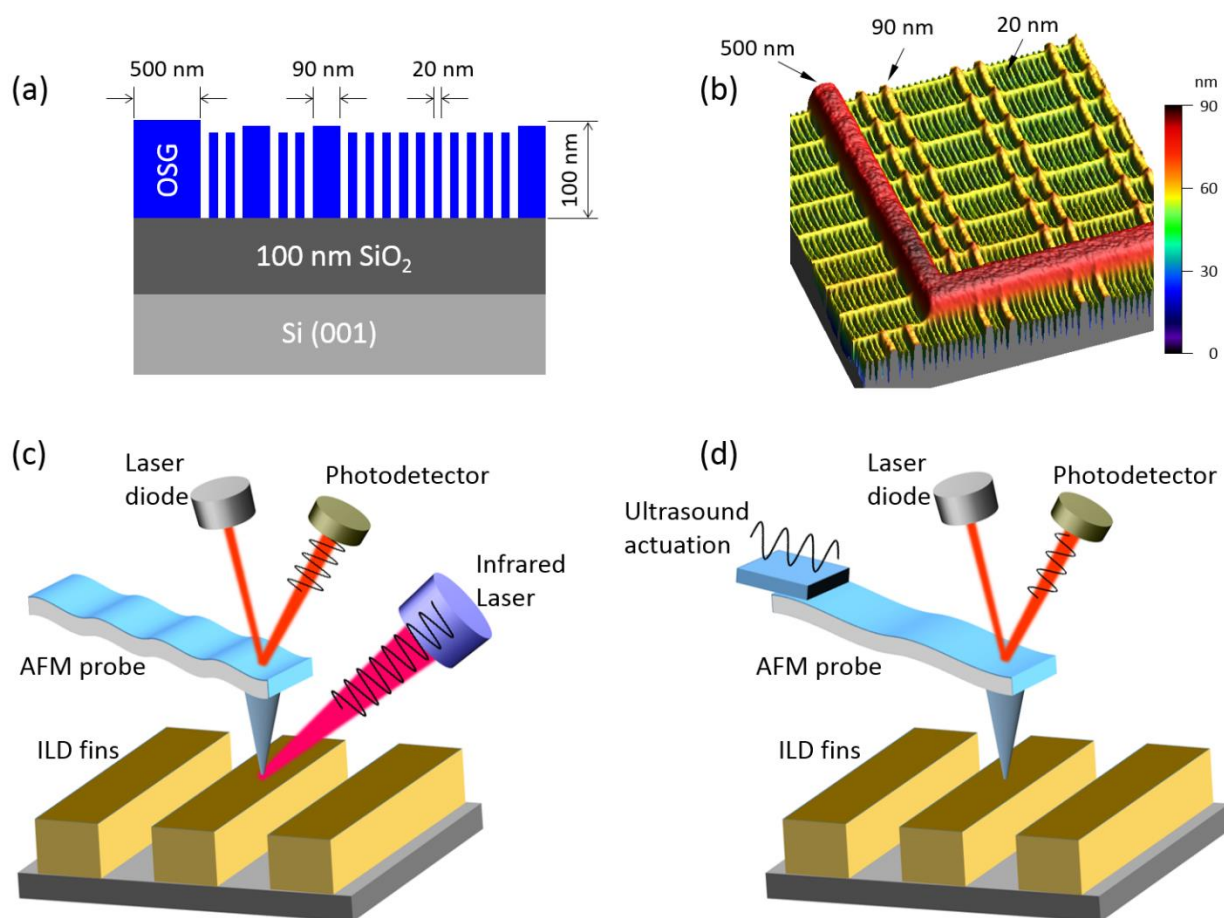


Figure 1. (a) Cross section schematic of the nano-porous organo-silicate (OSG) fin structures investigated in this study. (b) AFM image ($5 \mu\text{m} \times 5 \mu\text{m}$) of the surface topography of the actual structures investigated. (c) Schematic diagram of the AFM-IR measurements on the OSG fins. (d) Schematic diagram of the CR-AFM measurements on the OSG fins. Both (c) and (d) cartoons are drawn at relative scales to highlight the differences between the two techniques, with the impulse of the rapid sample expansion due to IR absorption causing a resonant oscillation of the AFM cantilever in AFM-IR (c) and the tip-sample contact mechanically vibrated at ultrasound frequencies in CR-AFM (d).

After completion of fin formation, some samples were exposed to a standard silylation treatment in an attempt to restore some of the terminal organic groups removed from the nano-

porous organo-silicate by the patterning process. The details of the silylation treatment are described elsewhere [37,38]. Additional samples completed a metallization process flow that filled the voids between the organo-silicate fins with Cu. This process consisted of first physically vapor depositing a TaN/Ta (TNT) barrier material followed by a Cu seed layer. The spaces between the fins were then completely filled with Cu via standard electroplating methods and a chemical mechanical polish was utilized to remove the Cu overburden leaving exposed the top of the nano-porous organo-silicate fins as well as the TNT and Cu surfaces [39].

AFM-IR, CR-AFM & FTIR Characterization

To follow changes in the chemical structure and mechanical properties of the nano-porous organo-silicate induced by the pitch division patterning process as a function of feature size, we utilized the resonance enhanced mode of AFM-IR (Fig. 1c) [32] and CR-AFM (Fig. 1d) [34], respectively. In the resonance enhanced AFM-IR technique, a tunable IR laser is pulsed onto the sample of interest and thermal heating of the sample occurs when the IR wavelength coincides with the IR vibrational absorption bands characteristic of the material [24,27]. The photoinduced heating causes a thermal expansion of the sample that is then detected as an oscillation in an AFM probe tip in contact with the sample. The repetition rate of the IR laser is tuned to a contact resonance of the AFM cantilever to maximize the oscillation amplitude of the cantilever. By sweeping the IR laser over the wavelengths of interest and monitoring changes in the amplitude of the AFM probe tip ringing, an IR absorption spectrum can be obtained that is directly analogous to traditional transmission IR techniques such as Fourier-transform infra-red

(FTIR) spectroscopy [28,32]. The spatial resolution for this technique has been previously demonstrated to be as low as 15 – 20 nm [40,41].

For CR-AFM measurements, the tip-sample contact is mechanically vibrated at various frequencies to detect the so called “contact resonance frequencies”. These CR-frequencies are characteristic of the tip-sample contact stiffness (higher frequencies for stiffer contacts) and depend on the mechanical properties of the tip and sample, the contact geometry (e.g. spherical tip on a flat surface), and the applied force on contact [29]. By conducting CR-AFM measurements on different samples under the same conditions (same applied force and same contact geometry), differences between the mechanical properties (e.g. elastic modulus) of the samples are resolved. The spatial resolution of CR-AFM is determined by the contact radius established during measurements and it can be as small as 5-10 nm [33].

For the AFM-IR spectra presented here, a nanoIR2™ instrument was utilized. This instrument was equipped with a quantum cascade laser (QCL) and either an Arrow AFM probe with a force constant of 0.07 – 0.4 N/m (NanoandMore, Switzerland) or an Access-C AFM probe with a force constants between 0.06 – 0.9 N/m (AppNano, Mountain View, CA). The QCL was focused directly onto the sample at a polar angle of 30 ° and an approach angle of 60 ° from the front of the AFM probe, and swept continuously over the wavenumber range of interest [39]. The AFM-IR spectra were collected by tuning the repetition rate of the QCL to match a contact resonance of the AFM cantilever, typically the second flexural mode of the cantilever at ~180 kHz. This offers improved sensitivity over the OPO IR laser source used in previous investigations [32] and thus provides a better signal to noise ratio for the thermal low expansion of the organo-silicate material. The oscillation amplitude of the probe at this frequency was then plotted versus the wavelength of the QCL to generate spectra. All experimental data were

collected with the AFM probe in the contact mode using Analysis Studio software (Version 3.7, Anasys Instruments, Santa Barbara, CA) [37].

For comparison, transmission FTIR spectra were collected from the nano-porous organo-silicate film before patterning using a Thermo Scientific Nicolet 6700 FTIR spectrometer and deuterated L-alanine doped triglycine sulfate (DLATGS) detector. The spectra were acquired from 400 – 7000 cm^{-1} with 4 cm^{-1} resolution and signal averaged over 128 scans. The absorption spectrum of the Si substrate and thin film-substrate optical interference effects were removed using rigorous methods that accounted for the full wave nature of light and have been previously described in detail [42,43].

For CR-AFM, single-point measurements were performed on the unpatterned blanket organo-silicate film and the 500 and 90 nm patterned fins by mechanically vibrating the tip-sample contact from the base of the cantilever [34]. The AFM probe used for these measurements was a SEIH PPP probe (NanoSensors, Neuchatel, Switzerland) with the free (out of contact) first eigenmode frequencies at 102.7 kHz and 642.6 kHz, respectively; the cantilever's spring constant was determined to be 7.35 ± 0.05 N/m by Laser Doppler Vibrometer. A lock-in amplifier with an internal signal generator (Signal Recovery AMETEK, Oak Ridge, TN) was used to vibrate the AFM cantilever and detect the AFM photodiode signal (MultiMode 8, Bruker, Santa Barbara, CA) at the oscillation frequency. For each measurement, the tip was brought into contact at a setpoint of 60 nN applied force and the frequency of the imposed modulation was swept from 100 kHz to 2 MHz with a step of 250 Hz [33,34]. The elastic modulus calculations were made by considering the blanket film as a reference with the modulus of 3.5 GPa and reporting all the measured contact stiffnesses to the contact stiffness measured on the blanket film; the tip-sample contacts were treated as Hertz contacts [33].

RESULTS AND DISCUSSION:

To monitor changes in the chemical structure of the organo-silicate fins induced by the patterning process, AFM-IR was used to focus specifically on relative changes in absorbance for the symmetric SiC-H₃ deformation mode at $\sim 1270\text{ cm}^{-1}$ which correlates directly with the concentration of terminal CH₃ groups present in the nano-porous organo-silicate structure. As has been detailed by many others [44], the incorporation of terminal organic groups within a silicate material radically disrupts the Si-O-Si network bonding and forces a more open / lower density structure to be adopted along with the creation of nano-pores of varying size and interconnectivity. Numerous additional blanket/unpatterned film studies have shown a direct correlation between the concentration of such terminal organic groups, porosity and mechanical properties [45,46]. In this regard, Figure 2a presents AFM-IR spectra of the symmetric SiC-H₃ deformation band collected from both the 20, 90, and 500 nm wide fins after completion of the pitch division patterning process. Also included in Fig. 2a is a micron-scale resolution transmission FTIR spectrum collected from an unpatterned thin film of the same nano-porous organo-silicate [34]. To better facilitate a direct comparison, the IR spectra in Figure 2a were all scaled / normalized to have the same absorbance for the Si-O-Si stretching band at 1050 cm^{-1} (not shown in order for the relative changes in the lower absorbance SiC-H₃ deformation band to be more easily observed). As can be seen, the absorbance for the SiC-H₃ deformation band decreases for the patterned vs. unpatterned porous organo-silicate and the absorbance decreases further as the width of the fin decreases. For both the 20 and 90 nm wide fins, the SiC-H₃ deformation band is almost below the AFM-IR detection limits.

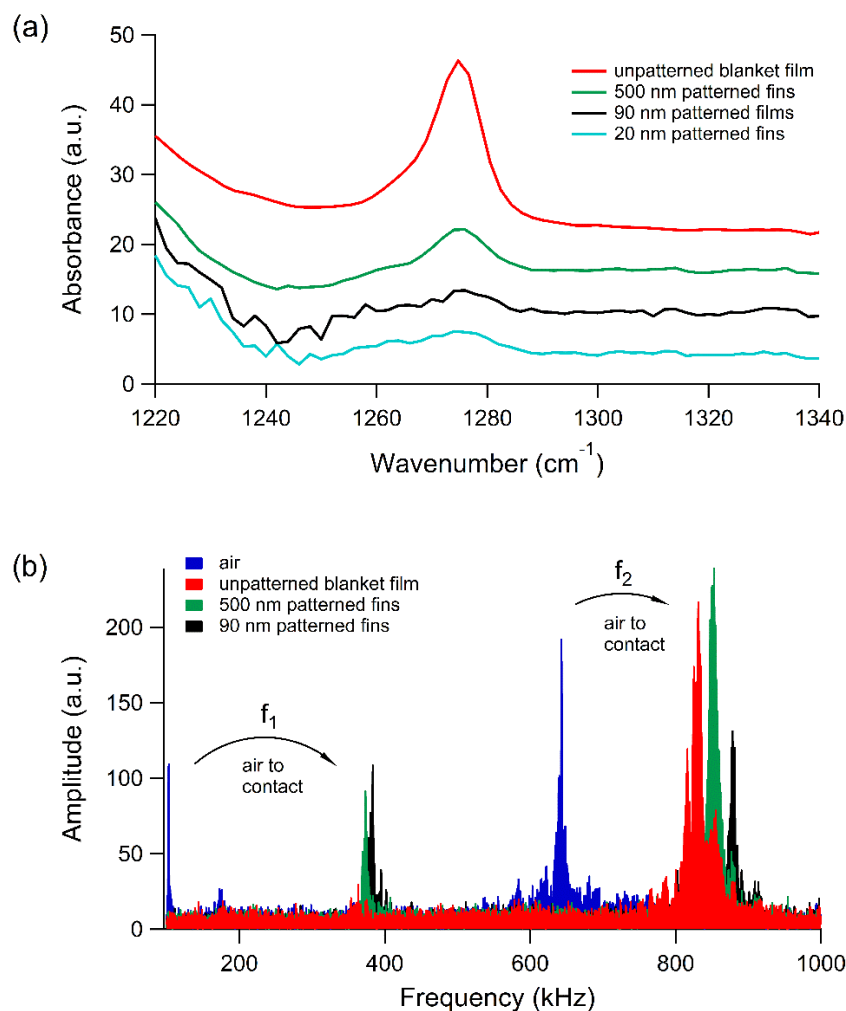


Figure 2. (a) Transmission FTIR and AFM-IR spectra of the symmetric SiC-H₃ deformation mode from a nano-porous organo-silicate unpatterned film and patterned fins (widths of 500 nm, 90 nm, and 20 nm), respectively. (b) CR-AFM spectra at 60 nN applied force of the first two eigenmodes from the same unpatterned film, 500 nm fins, and 90 nm fins that were measured in (a). The arrows indicate the frequency shifts of the two eigenmodes from air to contact.

The loss of terminal SiC-H₃ groups is attributed to abstraction of terminal organic groups by both the plasma etch utilized to transfer the photolithographically defined pattern and the plasma ash and wet cleans utilized to remove the hardmask and polymeric plasma etch residues

after the plasma etch [32,46-48]. The correlation between the decrease in the SiC-H₃ absorbance and fin width is attributed to the limited penetration depth and diffusion length for the ions, radicals and other chemically active species present in the plasma etch, ash, and wet cleans through the overlying hard mask and interconnected porosity in the organo-silicate. More specifically, as the fin dimensions decrease, the penetration depth and diffusion length start to represent an increasingly larger percentage of the fin width. The near complete disappearance of the Si-CH₃ deformation band for the 20 and 90 nm wide fins suggests that the penetration depth and diffusion lengths in this case are on the order of 10 - 100 nm. This length scale range is consistent with both prior experimental and theoretical investigations of O radical diffusion and CH₃ depletion in blanket thin film/unpatterned nano-porous organo-silicate dielectrics [32,49]. We also note that while CH₃ abstraction could likely be observed via transmission FTIR measurements of the same macro structures, the feature size dependence would have not been observed due to the diffraction limited micron scale resolution of this technique.

To complement the above chemical structure spectroscopy, CR-AFM measurements were additionally performed on the same nano-porous fin structures to assess relative differences in mechanical properties [50]. In Figure 2b, CR frequency spectra are shown for the unpatterned blanket film and the 500 and 90 nm fins that were acquired under the same applied force of 60 nN. Specifically, it is shown how the first two eigenmode frequencies of the cantilever shift from air (out of contact) to contact on each of the samples, with the largest shift on the 90 nm fins. The increase in the CR frequency shifts on patterned fin structures relative to the unpatterned/blanket film indicates a clear stiffening of the patterned nano-porous organo-silicate compared with the unpatterned thin film, which points to a width dependence of the mechanical stiffness analogous to that of the IR absorbance. The direct relationship between the observed CR frequency shifts

and the stiffness of the materials in Figure 2b is supported by the requirement of preserving the same contact geometry, namely spherical tip of the same radius on flat surface, during measurements. This was verified by the consistent results obtained over three alternative rounds of 10 measurements on each material. However, the CR-AFM measurements on 20 nm wide fins were not included in this discussion because the edge compliances have a significant contribution in this case [42], and a direct comparison with the CR-AFM measurements on the wider fins would therefore be inconsistent.

The decrease in SiC-H₃ absorbance and increase in the elastic modulus as a function of fin width are summarized in Figure 3. In terms of elastic modulus, the 500 nm and 90 nm fins, when considered as homogeneous structures exhibit increases of 14% and 40%, respectively, with respect to the 3.5 GPa modulus of the unpatterned blanket film [34]. Both the increase in elastic modulus and decrease in SiC-H₃ absorbance with the decrease in fin width suggest a conversion of the hybrid nano-porous organo-silicate fins to a stiffer SiO_x matrix [48]. In fact, additional depth-dependent CR-AFM measurements [42] and detailed modeling to include possible structural inhomogeneities and edge compliances have shown that about 20 nm of the top and sidewalls of the 90 nm fins consist of a thin “crust” layer with increased stiffness ($E = 7.9 \pm 2.2$ GPa) relative to the remaining bottom portion of the fin that has mechanical properties closer to the unpatterned organo-silicate ($E = 3.4 \pm 0.8$ GPa). The analysis also showed that the volume of the 20 nm fins is almost entirely stiffened with a modulus of $E = 9.8 \pm 1.7$ GPa (refer to Figure 3). The elastic modulus values determined here for the stiffer regions of the fins are comparable with the elastic modulus determined in a previous study for the SiO_x matrix structure of these porous organo-silicate materials ($E = 7.3 \pm 0.2$ GPa). It is therefore conclusive that the length scale for CH₃ abstraction from the organo-silicate by the patterning process is closer to the

order of 10-20 nm and that fins of 20 nm or smaller will be almost completely depleted of CH_3 during processing.

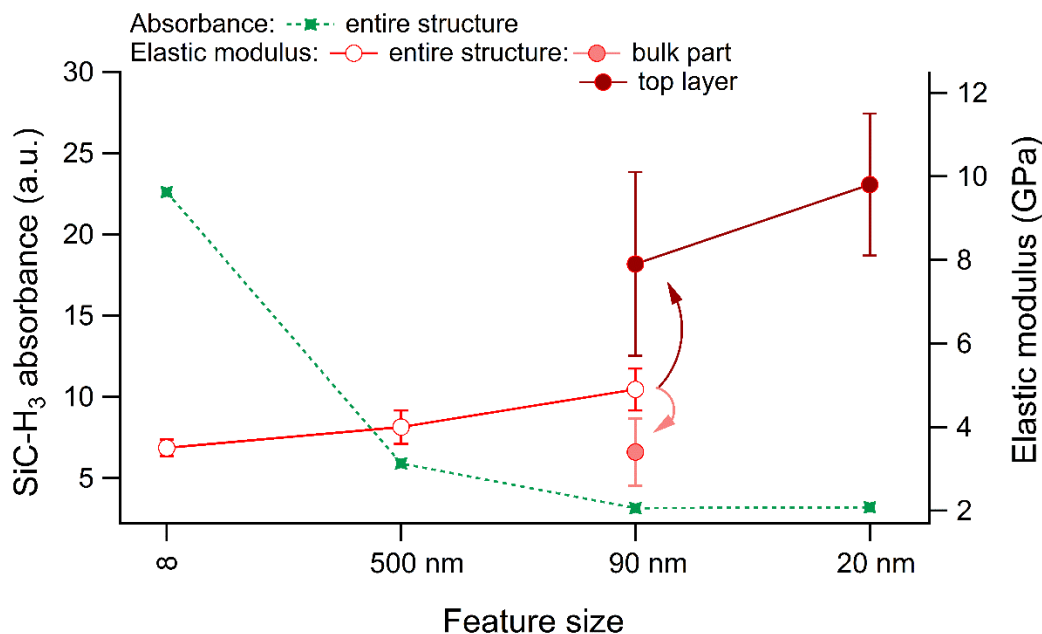


Figure 3. SiC-H₃ absorbance (AFM-IR) and Young's modulus (CR-AFM) as a function of feature size for unpatterned and patterned nano-porous organo-silicates. Note: the error bars for the AFM-IR SiC-H₃ absorbance represents the maximum variability observed from spectra acquired at different sites with the same feature size. The details of the errors associated with the CR-AFM Young's modulus measurements are covered in [34].

While the abstraction of terminal organic groups from the matrix of the nano-porous organo-silicate clearly results in a slight stiffening of the fins, it also results in the incorporation of significant amounts of hydroxyl groups (Si-OH) that can increase both the dielectric constant/capacitance and electrical leakage of nano-porous organo-silicate dielectrics [51]. This is typically counteracted by converting the hydroxyl groups back to terminal organics via a chemical silylation process that utilizes various alkoxysilane or organosilazanes and takes

advantage of the intrinsic porosity present to allow the silylating agent to easily penetrate the silicate matrix and react with hydroxyl groups [35]. To further examine the correlation between terminal Si-CH₃ concentration and local mechanical properties, the previously examined fin structures were given such an industry standard silylation treatment [35,36]. Figure 4 provides a comparison of the AFM-IR spectra from the 20 and 500 nm wide fins both before and after the silylation treatment. As shown in Fig. 4a (refer to curves i and ii), there was a clear overall increase in absorbance for the SiC-H₃ deformation band after the silylation treatment for the 20 nm wide fins. In particular, the absorbance specifically increased at ~ 1265 cm⁻¹ which is indicative of an increase in (CH₃)₂SiO₂ entities as opposed to CH₃SiO₃ entities represented by absorbance at 1275 cm⁻¹ [44]. The increase in (CH₃)₂SiO₂ entities after the silylation treatment is fully consistent with and expected based on the structure of the silylation agent that includes two terminal CH₃ groups [35,36].

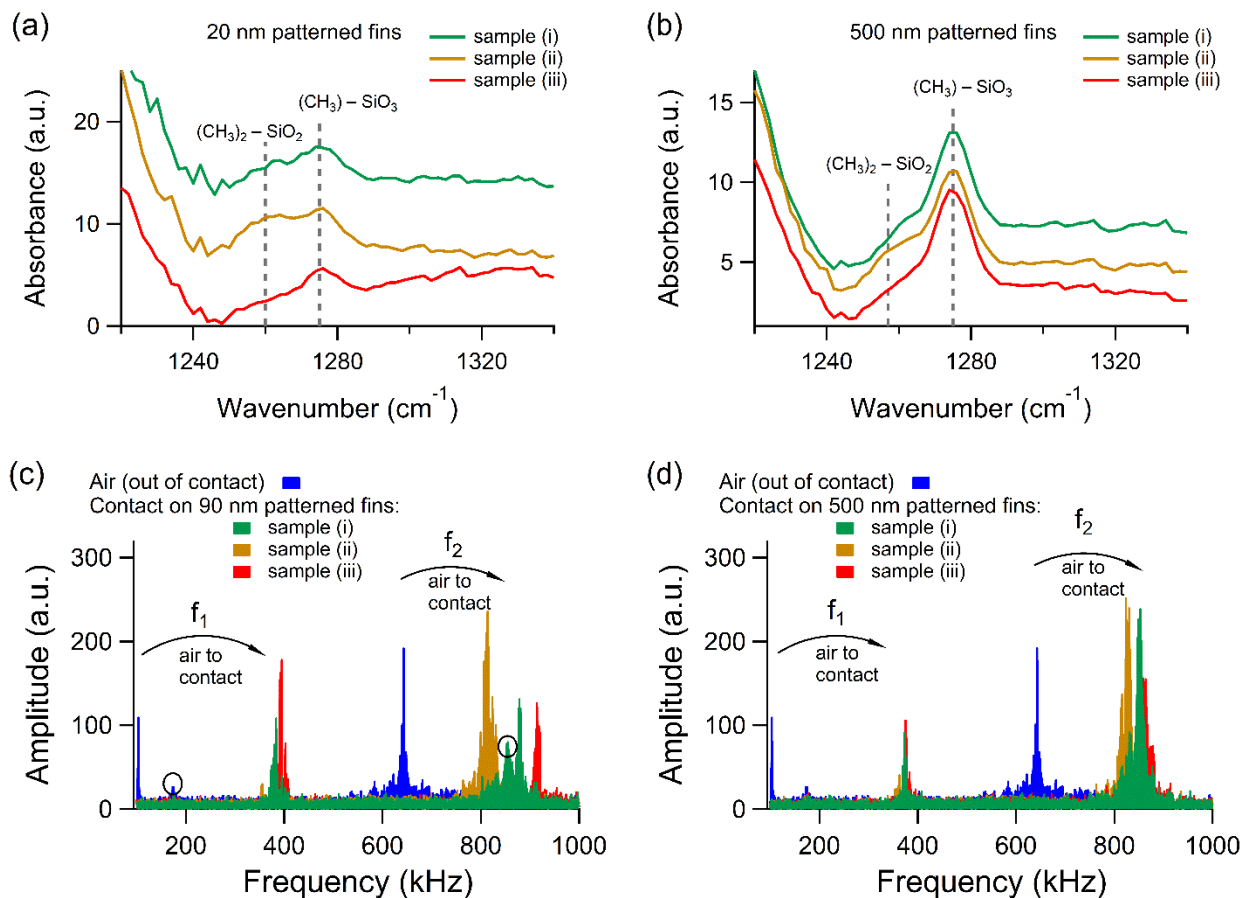


Figure 4. (a) and (b) AFM-IR spectra of the symmetric SiC-H₃ deformation mode from the patterned nano-porous organo-silicate fins with widths of 20 nm and 500 nm, respectively. (c) and (d) CR-AFM spectra of the first two eigenmodes from the patterned nano-porous organo-silicate fins with widths of 90 nm and 500 nm, respectively; the circled peaks were observed in all the measurements and isolated as spurious resonances. The sample labeling is: (i) after pattern transfer, (ii) after chemical silylation treatment, and (iii) after metallization process flow.

In contrast, relatively little change was observed in the AFM-IR spectra of the 500 nm wide fins after the chemical silylation treatment. As shown in Fig. 4b (refer to curves i and ii), the CH_3SiO_3 absorbance at 1275 cm^{-1} was relatively unchanged and only a slight increase at 1265 cm^{-1} indicative of $(\text{CH}_3)_2\text{SiO}_2$ entities was observed. This is consistent with the 500 nm fins exhibiting both reduced SiCH_3 loss and reduced stiffening induced by the patterning process relative to the 20 and 90 nm wide fins. Specifically, the reduced abstraction of terminal CH_3 groups and creation of a SiO_x damage/crust layer presented fewer hydroxyl species for the silylation agent to react with during the silylation treatment.

To assess the impact of the silylation treatment on the mechanical properties of the organo-silicate fin structures, CR-AFM measurements were again performed. These measurements interestingly showed a decrease in contact resonance frequency relative to the pre-silylation values. The stiffness decrease is more significant for the 90 nm fins (refer to curves i and ii in Fig. 4c) than for the 500 nm fins (refer to curves i and ii in Figure 4d); the effect is visible on both CR eigenmodes and corresponds to a decrease in the elastic modulus of 37% for the 90 nm fins and 15% for the 500 nm fins with respect to the elastic moduli of the samples after pattern transfer (curves i in Figs. 4c and 4d) (in these calculations the fins were considered as homogeneous structures). This observation is fully consistent with the AFM-IR results showing a partial restoration of terminal Si-CH_3 groups and is also consistent with the likely partial repair of the SiO_x damage/crust layer created on the top surface of the fins by the patterning process. These results thus further confirm the chemical structure-mechanical property correlation between terminal CH_3 groups and the modulus/mechanical properties of the nanoporous organo-silicate.

To further strengthen the observed chemical structure-mechanical property relationship, the silylated nano-porous organo-silicate fins were exposed to additional plasma and wet chemical processes to fill the spaces between the fins with Cu as in a typical state-of-the-art metal interconnect structure. This process flow specifically consisted of plasma cleaning, physical vapor deposition (PVD), chemical mechanical planarization (CMP) and wet chemical cleaning steps that have all shown the potential to remove terminal organic groups from the matrix of nano-porous organo-silicate dielectrics in a similar fashion as observed previously by the pattern transfer process [31,52,53]. This is clearly shown Fig. 4a (curve iii) where the additional metallization processing also resulted in a decrease in SiC-H₃ absorbance detected by AFM-IR from the 20 nm wide fin structures and that largely negated the effects of the silylation treatment. In contrast, the AFM-IR spectra from the 500 nm wide fin structures (curve iii in Fig. 4b) were again relatively unchanged by the metallization process flow. This suggests a similar feature size dependence for abstraction of terminal CH₃ groups from the nano-porous organo-silicate material. More importantly, CR-AFM measurements performed on the nano-porous organo-silicate fins showed an increase in contact resonance frequency almost back to the values observed after the pattern transfer process (refer to curves iii in Figs. 4c and d), with an increase of about 25% for the 90 m fins and 5% for the 500 nm fins with respect to the elastic moduli of the samples after pattern transfer (curves i in Figs. 4c and 4d) (in these calculations the fins were considered as homogeneous structures). This further confirms and strengthens the chemical structure-mechanical property correlation between terminal CH₃ and stiffness for nano-porous organo-silicates.

CONCLUSION:

In conclusion, it has been demonstrated that AFM-IR and CR-AFM can be combined to perform chemical structure-mechanical property characterization at the nanoscale. For the specific case examined here, a direct correlation has been observed between the removal and reinsertion of terminal organic groups and the elastic modulus for nano-patterned organo-silicate fins. Specifically, an inverse correlation between terminal organic concentration and elastic modulus was observed where selective removal of the organic component by plasma etching/ashing resulted in a stiffness increase and reinsertion via chemical silylation resulted in a stiffness decrease. Examination of this effect as a function of fin width further showed that the loss of terminal organics and stiffness increase occurred primarily at the exposed top and sidewall surfaces of the nano-porous organo-silicate fins over a length scale of 10-20 nm. We believe these results provide a compelling case study for other material systems where the observation of similar nanoscale structure-property relationships may be essential in developing new materials or increasing understanding of nanoscale size effect phenomena.

ACKNOWLEDGEMENTS:

The authors would like to acknowledge Marie Tripp for support of the measurements at Anasys. The authors would also like to acknowledge the support and encouragement from Drs. B. Tufts, J. Maiz, and B. Boyanov of Intel Corporation during the course of this research. Anasys Instruments would like to acknowledge SBIR funding from the National Science Foundation (grants 1126871 and IIP-1152308).

DISCLAIMER:

Certain commercial equipment, instruments or materials are identified in this document. Such identification does not imply recommendation or endorsement by the National Institute of Standards and Technology or Intel Corporation, nor does it imply that the products identified are necessarily the best available for the purpose.

REFERENCES:

1. Miodownik, M. *Stuff Matters*, Houghton Mifflin Harcourt, Boston, 2014.
2. Callister, Jr. W.D.; Rethwisch, D.G., *Materials Science and Engineering an Introduction*, John Wiley & Sons Inc., Hoboken, NJ, 2010.
3. Weiss, P. *ACS Nano* **2012**, *6*, 1877-1879.
4. Moon, R. ; Martini, A.; Nairn, J.; Simonsen, J.; Youngblood, J. *Chem. Soc. Rev.* **2011**, *40*, 3941-3994.
5. Dosch, H. *Appl. Surf. Sci.* **2004**, *182*, 192-195.
6. Kelsall, R.; Hamley, I.; Geoghegan, M. *Nanoscale Science and Technology* (John Wiley & Sons Ltd., West Sussex, 2005).
7. International Technology Roadmap for Semiconductors (ITRS): 2009 (Semiconductor Industry Association, San Jose, CA, 2009).
8. King, S.; Simka, H.; Herr, D.; Akinaga H.; Garner, M. *APL Mater.* **2013**, *1*, 040701-8.

9. Rohrer, G.; Affatigato, M.; Backhaus, M.; Bordia, R.; Chan, H.; Curtarolo, S.; Demkov, A.; Eckstein, J.; Faber, K.; Garay, J.; Gogotsi, Y.; Huang, L.; Jones, L.; Kalinin, S.; Lad, R.; Levi, C.; Levy, J.; Maria, J.; Mattos Jr., L.; Navrotsky, A.; Orlovskaya, N.; Pantano, C.; Stebbins, J.; Sudarshan, T.; Tani, T.; Weil, K. *J. Am. Ceram. Soc.* **2012**, *95*, 3699-3712.
10. Tetard, L.; Passian, A.; Farahi, R.; Thundat, T.; Davison, B. *Nat. Nanotechnol.* **2015**, *10*, 870-878.
11. Suresh, S. *J. Mater. Res.* **2006**, *21*, 1871-1877.
12. Morozovska, A.; Eliseev, E.; Svechnikov, G.; Kalinin, S. *Phys. Rev. B* **2011**, *84*, 045402-20.
13. Le, T.; Epa, V.; Burden, F.; Winkler, D. *Chem. Rev.* **2012**, *112*, 2889-2919.
14. Zhang, X.; Jenehke, S.; Perlstein, J. *Chem. Mater.* **1996**, *8*, 1571-1574.
15. Hammiche, A.; Pollock, H.; Price, D.; Reading, M. *Int. J. Pharmaceutics* **1999**, *192*, 85-96.
16. Majumder, A. *Ann. Rev. Mater. Sci.* **1999**, *29*, 505-585.
17. Geiss, R.; Hurley, D.; Kos, A.; Kopcinska-Müller, M. *Meas. Sci. Technol.* **2005**, *16*, 2167-2172.
18. Yablon, D.; Gannepalli, A.; Proksch, R.; Killgore, J.; Hurley, D.; Grabowski, J.; Tsou, A. *Macromolecules* **2012**, *45*, 4363-4370.
19. Natelson, D. *ACS Nano* **2012**, *6*, 2871-2876.
20. Widawsky, J.; Kamenetska, M.; Klare, J.; Nuckolls, C.; Steigerwald, M.; Hybertsen, M.; Venkataraman, L. *Nanotechnology* **2009**, *20*, 434009-6.
21. Jalili, N.; Laxminarayana, K. *Mechatronics* **2004**, *14*, 907-945.
22. Vertikov, A.; Kuball, M.; Nurmikko, A.; Maris, H. *Appl. Phys. Lett.* **1996**, *69*, 2465-2467.
23. Henn, M.; Gross, H.; Heidenreich, S.; Scholze, F.; Elster, C.; Bar, M. *Meas. Sci. Technol.* **2004**, *25*, 044003-9.

24. Dazzi, A.; Glotin, F.; Ortega, J. M.; Prazeres, R. *Ultramicroscopy* **2007**, *107*, 1194-1200.
25. Huth, F.; Schnell, M.; Wittborn, J.; Ocelic, N.; Hillenbrand, R. *Nat. Mater.* **2011**, *10*, 352-356.
26. Xu, X.; Rang, M.; Craig, I.; Raschke, M. *J. Phys. Chem. Lett.* **2012**, *3*, 1836-1841.
27. Lu, F.; Belkin, M. *Opt. Express* **2011**, *19*, 19942–19947.
28. Dazzi, A.; Prater, C.; Hu, Q.; Chase, D.; Rabolt, J.; Marcott, C. *Appl. Spectr.* **2012**, *66*, 1365-1384.
29. Stan G.; King, S.; Cook, R.; *J. Mater. Res.* **2009**, *24*, 2960-2964.
30. Maex, K.; Baklanov, M.; Shamiryman, D.; Iacopi, F.; Brongersma, S.; Yanovitskaya, Z. *J. Appl. Phys.* **2003**, *93*, 8793-8841.
31. Baklanov, M.; de Marneffe, J.; Shamiryman, D.; Urbanowicz, A.; Shi, H.; Rakhimova, T.; Huang, H.; Ho. P. *J. Appl. Phys.* **2013**, *113*, 041101-41.
32. Hu, Q.; Kjoller, K.; Myers, A.; Singh, K.; King, S. *Vib. Spect.* **2016** *86*, 223-232.
33. Stan, G., King, S., Cook, R. *Nanotechnology* **2012**, *23*, 215703-9.
34. Stan, G.; Mays, E.; Yoo, H.; King, S. *Nanotechnology* **2016**, *27*, 485706-9.
35. Chawla, J.; Singh, K.; Myers, A.; Michalak, D.; Schenker, R.; Jezewski, C.; Krist, B.; Gstrein, F.; Indukuri, T.; Yoo, H. *Proc. SPIE* **2014**, *9054*, 905404-8.
36. Bailey, S.; Mays, E.; Michalak, D.; Chebiam, R.; King, S.; Sooryakumar, R. *J. Phys. D: Appl. Phys.* **2013**, *46*, 045308-7.
37. Oszinda, T.; Schaller, M.; Schulz, S.E. *J. Electrochem. Soc.* **2010**, *157*, H1140-H1147.
38. Imada, T.; Nakata, Y.; Ozaki, S.; Kobayashi, Y.; Nakamura, T. *Jpn. J. Appl. Phys.* **2015**, *54*, 71502-5.

39. Lo, M.; Dazzi, A.; Marcott, C.; Dillon, E.; Hu, Q.; Kjoller, K.; Prater, C.; King, S. *ECS J. Solid State Sci. Technol.* **2016**, *5*, P3018-P3025.
40. Felts, J.; Cho, H.; Yu, M.; Bergman, L.; Vakakis, A.; King, W. *Review of Scientific Instruments* **2013**, *84*, 023709-6.
41. Katzenmeyer, A.; Holland, G.; Kjoller, K.; Centrone, A. *Anal. Chem.* **2015**, *87*, 3154-3159.
42. King, S.; Milosevic, M. *J. Appl. Phys.* **2012**, *111*, 073109-9
43. Milosevic, M.; King, S. *J. Appl. Phys.* **2012**, *112*, 093514-7.
44. Gates, S.; Neumayer, D.; Sherwood, M.; Grilla, A.; Wang, X.; Sankarapandian, M. *J. Appl. Phys.* **2007**, *101*, 094103-8.
45. Yeap, K.; Kopycinska-Mueller, M.; Chen, L.; Chen, Y.; Jungmann, M.; Krause-Rehberg, R.; Mahajan, S.; Vlassak, J.; Gall, M.; Zschech, E. *J. Mater. Res.* **2013**, *28*, 1262-1268.
46. Guo, X.; Jakes, J.; Banna, S.; Nishi, Y.; Shohet, J. *J. Appl. Phys.* **2014**, *116*, 044103-9.
47. Darnon, M.; Chevolleau, T.; David, T.; Posseme, N.; Ducote, J.; Licitra, C.; Vallier, L.; Joubert, O.; Torres, J. *J. Vac. Sci. Technol. B* **2008**, *26*, 1964-70.
48. Myers, J.; Zhang, X.; Bielefeld, J.; Lin, Q.; Chen, Z. *J. Phys. Chem. B* **2015**, *119*, 1736-1746.
49. Goldman, M.; Graves, D.; Antonelli, G.; Behera, S.; Kelber, J. *J. Appl. Phys.* **2009**, *106*, 013311-7.
50. Stan, G.; Gates, R.; Kavuri, P.; Torres, J.; Michalak, D.; Ege, C.; Bielefeld, J.; King, S. *Appl. Phys. Lett.* **2014**, *105*, 152906-4.
51. Kubasch, C.; Klaus, C.; Ruelke, H.; Mayer, U.; Barha, J. W. *IEEE Trans. Elect. Dev.* **2010**, *57*, 1865-1872.
52. Gates, S.; Rao, S.; Anandan, V.; Krishnan, M.; Cohen, S.; Ostrovski, Y.; Klymko, N.; Chace, M.; Canaperi, D. *Microelectron Eng.* **2012**, *91*, 82-88.

53. Inoue, N.; Furutake, N.; Ito, F.; Yamamoto, H.; Takeuchi, T.; Hayashi, Y.; *Jpn. J. Appl. Phys.* **2008**, *47*, 2468-2472.